1997-8-5

Simulation of Chaotic Particle Motion in Particle-Laden Jetflow and Application to Abrasive Waterjet Machining

Z. Yong
Senior Researcher. Mem. ASME

R. Kovacevic
Professor. Mem. ASME

Center for Robotics and Manufacturing Systems, University of Kentucky, Lexington, KY 40506-0108

A novel method is presented for modeling the abrasive waterjet machining process. Particle motion on the cross section of particle-laden jetflow is simulated in order to quantify the erosion contributions of millions of particles having different kinematic behaviors. The simulation is performed using fractal point sets with chaotic behavior for the cases of circular and noncircular (elliptical, triangular) jets. The jetflow constructed can be endowed with any desired velocity profile and/or particle flowrate. In association with a classical constitutive equation for estimating the penetration ability of a particle, the drilling and cutting operations are simulated and verified by experiment for titanium, glass, and other materials. Roughness and waviness of the cutting surfaces are also simulated and there is good consistency between theory and experiment. Triangular and elliptical jetflows are utilized to explore potential applications of noncircular abrasive waterjets.

1 Introduction

In general, there are two fundamental issues in modeling and simulation of three-dimensional (3D) abrasive waterjet (AWJ) machining. One is to find the constitutive equation—the relation between the depth of penetration by a high speed abrasive particle and other machining parameters, including the jet speed, material property, impact angle, surface geometry, etc. The other is to quantify the dynamic nature of particle-laden jetflow, reflecting disordered particle motion, the influence of nozzle geometry and movement, and characteristics of three-phase flow such as laminar and turbulent velocity profiles. The first issue focuses on the local erosion rate by individual particles while the second one emphasizes the global description of surface formation. For instance, waviness on lateral surfaces of cut is not affected by the erosion rate of a single particle, but does depend on the nozzle speed and total depth of cut. Evidence for this claim is that similar waviness also occurs in laser and other beam cutting processes.

To date, much attention has been paid to the first issue and remarkable progress has been achieved by scholars and engineers regarding different impact conditions (Finnie, 1958; Bitter, 1962; Neilson and Gilchrist, 1967; Tilly and Sage, 1970; Hutchings, 1979; Gulden, 1979; Hashish, 1984; Zeng and Kim, 1992; Yong and Kovacevic, 1997a). However, the results of single particle analysis alone are not enough to precisely describe an on-line AWJ machining process. In addition, the trajectories of millions of particles with chaotic dynamic behavior must be quantitatively described.

Particles in AWJ differ greatly from each other in terms of their velocities and positions at different moments, and most importantly, their disordered behavior directly affects the depth of cut as well as the surface quality. In fact, because of the lack of a theoretical basis for the particle motion in jetflow, namely the second issue, empirical models to date are incapable of reflecting many important characteristics of a kerf, such as 3D surface configuration, roughness and waviness as well as the machining parameters that influence them like the traverse speed of a nozzle. In addition, conventional models break down when engineers and researchers change nozzle shapes (Hongawa et al., 1992; Hashish, 1994; Rankin and Wu, 1995) from a circular one to noncircular ones, or when they use alternative techniques during a machining operation, such as rotating a nozzle along with the straight movement, or accelerating and decelerating it for controlling the depth of cut.

It is essential for a robust model to balance the weight of two research orientations. At present, it is impractical to establish a series of nonlinear partial differential equations for describing locations and velocities of particles simply because researchers are still struggling with the accurate analysis of turbulence in one-phase flow. However, in order to model and simulate an AWJ machining process, it is virtually impossible to avoid such an analysis since the cutting action in AWJ machining is actually the result of the accumulation of an enormous number of tiny craters and/or ditches generated by particles, as shown in Figs. 1–2. This suggests that a new approach must be developed to meet practical needs.

The strategy adopted in the present research is to simulate particle motion on the cross section of a particle-laden jetflow by using fractal point sets with chaotic features. Here a point represents a particle and its coordinates define the position of the particle. It is important to point out that a general point set is not directly applicable unless it satisfies strict physical and mathematical constraints. For example, it should be able to have any desired velocity profile and flowrate, be suitable to any nozzle shape, and possess global axisymmetry and uniformity. After desired particle-laden flow is constructed, several AWJ machining operations are simulated and compared with experimental data. The results show that the approach developed is very effective and industrially applicable as an optional tool to reduce expensive and time-consuming tests.

2 Simulation of Particle Motion

In light of the physical and geometric conditions forming three-phase flow (abrasives, water and air) in the mixing tube, three assumptions are introduced to describe the characteristics of particle motion in a circular cross section of the multiphase flow. First, the appearance of particles on the cross section is

Contributed by the Fluids Engineering Division for publication in the JOURNAL OF FLUIDS ENGINEERING. Manuscript received by the Fluids Engineering Division August 3, 1995; revised manuscript received January 12, 1997. Associate Technical Editor: M. W. Reeks.

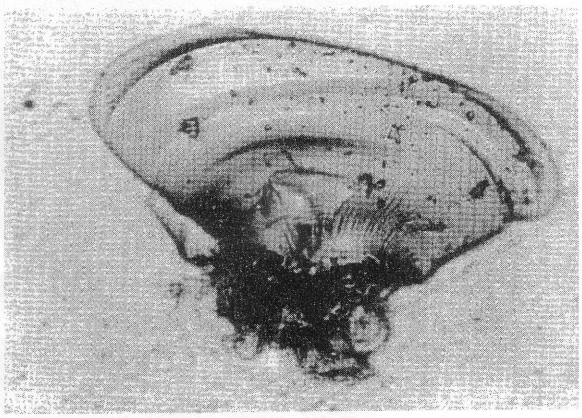

Fig. 1 A crater (X200) generated by an abrasive particle with average diameter 460 μm impinging on a glass plate

unpredictable or disordered for both laminar and turbulent flows. Second, globally speaking, the particle distribution on the cross section is approximately axisymmetrical after the particle number passing through the section exceeds a certain value. Third, the particle number through a subdomain of the cross section should be approximately equal to the particle number through another symmetric subdomain. The third feature is termed the global uniformity of particles. In the subsequent analysis, laminar and turbulent particle-laden flows are distinguished by their particle distribution and velocity profiles.

2.1 An Original Point Set. In order to describe instant particle motion on the cross section of particle-laden jetflow, a particle is assumed to be a mathematical point in space and its size and shape are not considered at this step. In this case, the key point for simulation is to find such a point set that possesses the above three features of particle motion on the cross section. After extensive examinations on the above three features of numerous fractal point sets under the Cartesian and polar systems, it is confirmed (Yong and Kovacevic, 1997b, c) that the following point set can be used to simulate the particle motion on the cross section of jetflow, given by

$$f_p = \{(x_1, y_1), (x_2, y_2), \ldots, (x_n, y_n)\} \quad (1)$$

$$= \{(r_1, \theta_1), (r_2, \theta_2), \ldots, (r_n, \theta_n)\} \subset J$$

$$0 \le r_n = (x_n^2 + y_n^2)^{1/2} \le 1 \quad (2)$$

$$0 \le \theta_n = \arctan\left(\frac{y_n}{x_n}\right) < 2\pi \quad (n = 0, 1, 2, \ldots) \quad (3)$$

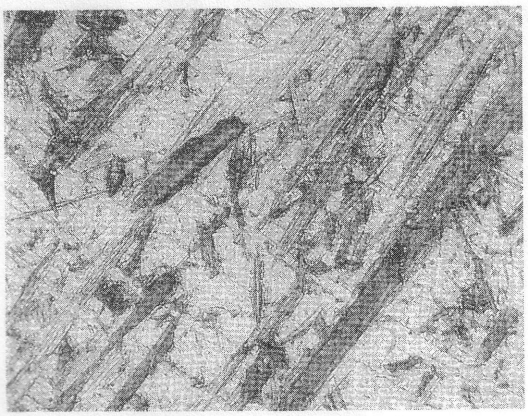

Fig. 2 Ditches (X200) on the titanium surface generated by particles

where $J = \{(\xi_1, \eta_1), (\xi_2, \eta_2), \ldots, (\xi_N, \eta_N)\}$ is a Julia set (fractal point set) produced by the nonlinear iterative equations

$$\xi_{N+1} = \{[R(\xi_N, \eta_N)]^2 + [I(\xi_N, \eta_N)]^2\}^{1/4} \cos[\theta(\xi_N, \eta_N)/2] - 0.368 \quad (4)$$

$$\eta_{N+1} = \{[R(\xi_N, \eta_N)]^2 + [I(\xi_N, \eta_N)]^2\}^{1/4} \sin[\theta(\xi_N, \eta_N)/2] + 0.4436 \quad (5)$$

with

$$R(\xi_N, \eta_N) = \xi_N^3 - 3\xi_N\eta_N^2 + 1.24(\eta_N^2 - \xi_N^2) \quad (6)$$

$$I(\xi_N, \eta_N) = -\eta_N^3 + 3\eta_N\xi_N^2 - 2.48\eta_N\xi_N \quad (7)$$

$$-\pi < \theta(\xi_N, \eta_N) = \arctan\left[\frac{I(\xi_N, \eta_N)}{R(\xi_N, \eta_N)}\right] \le \pi \quad (8)$$

$$x_n = 5\xi_N + 0.70, \quad y_n = 5\eta_N - 1.5 \quad (9)$$

Hereinafter, a particle on the cross section is positioned by the coordinates of a point, namely, a point in f_p will represent a particle. The particle distribution of f_p on a circular region and their unpredictable appearance are shown in Fig. 3 where the straight line connecting two points stands for the relative order of appearance of two particles. The axisymmetry and uniformity of f_p can be verified (Yong and Kovacevic, 1997b, c) by employing the rotating mapping function $T(\alpha) = e^{\alpha i}$ where α $(0 \le \alpha < 2\pi)$ is the rotating angle on the complex plane. Demonstration of the two properties are not displayed for compactness.

2.2 Velocity Profile of Point Set. After meeting three general properties of particle motion, the point set f_p is still not ready to represent particles on the cross section of particle flow because the velocity profile of f_p, along the normal direction of the cross section, may not be equivalent to that of particles. In the following, a governing equation for determining the velocity profile of f_p is introduced so that f_p can be endowed with any desired velocity profile. For the simplification of mathematical treatments, the mixture of particle, water, and air in jetflow is assumed to be uniform.

Based on the mass conservation principle, particles of f_p can be linked to their velocities through the equation

$$R_f = \frac{N_{xy}}{N_0} = \left(\int_{t_1}^{t} dt \iint_{S_{xy}} V_z ds\right) \Big/ \left(\int_{t_1}^{t_2} dt \iint_{S_0} V_z ds\right) \quad (10)$$

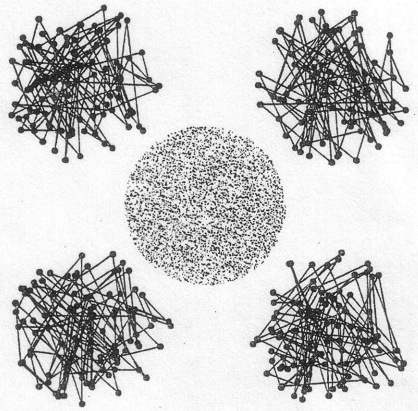

Fig. 3 Particle distribution on the circular region and their disordered appearance at different moments

giving

$$V_z = \left(\int_{t_1}^{t_2} dt \iint_{S_0} V_z ds \right) \frac{\partial^3 R_f}{\partial x \partial y \partial t} \tag{11}$$

In Eq. (10), R_f physically stands for the abrasive flowrate ratio; $V_z(t, x, y) = v_z/v_{z\max}$ is the dimensionless normal velocity of a particle at the point (x, y) and the instant t, v_z is the average normal velocity profile of the particle and $v_{z\max}$ is the maximum velocity of jetflow; S_{xy} is an arbitrarily-shaped subarea of the cross section S_0 of particle-laden jetflow; N_{xy} is the number of particles passing through S_{xy} in the time interval $t - t_1$ and N_0 is the number of particles passing through S_0 during $t_2 - t_1$. Note that when the jetflow is assumed to be steady and axisymmetrical Eq. (11) can be simplified to

$$V_z = \left(2\pi \int_0^1 V_z(r) r dr \right) \frac{\partial R_f}{r \partial r} \tag{12}$$

In terms of (10) and (12), the velocity profile V_z and flowrate ratio R_f of f_p are drawn in Fig. 4 and two analytical equations

$$V_z^* = (1 - r)^{1/10} \tag{13}$$

$$R_f^* = 1 - (1 - r)^{11/10}(1 + \tfrac{11}{10} r) \tag{14}$$

are also plotted as approximate representations of V_z and R_f. The irregularity of V_z and R_f results from the disordered nature of particles in f_p.

In most cases, abrasive waterjet can be treated as a steady flow and hence for simplicity in the subsequent discussion the velocity profile of particle-laden flow is considered as to be time-independent.

2.3 New Point Sets. When the off-line simulation needs a new particle source or point set $\bar{f}_p$ defined on an arbitrarily-shaped domain $\bar{S}_0$ with desired velocity profile $\bar{V}_z$, and/or flowrate ratio $\bar{R}_f$, the mapping technique is applied to convert f_p into $\bar{f}_p$ through the integral equation

$$R_f = \bar{R}_f \Leftrightarrow \left(\iint_{S_{xy}} V_z^* ds \right) \Big/ \left(\iint_{S_0} V_z^* ds \right) = \left(\iint_{\bar{S}_{xy}} \bar{V}_z ds \right) \Big/ \left(\iint_{\bar{S}_0} \bar{V}_z ds \right) \tag{15}$$

where the subdomain $\bar{S}_{xy}$ or $\bar{S}_0$ contains unknown coordinates (x, y) or (r, θ) of particles in $\bar{f}_p$. The physical meaning of (15) is that corresponding to a group of points in S_{xy}, another group of particles in $\bar{S}_{xy}$ is determined through (15) which possesses the velocity profile $\bar{V}_z(x, y)$.

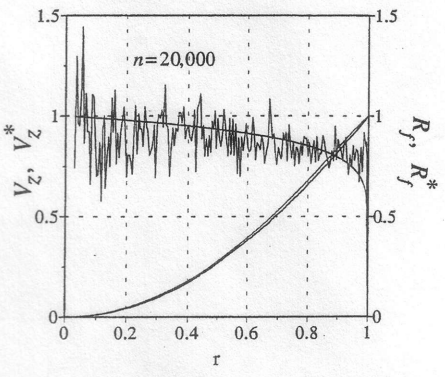

Fig. 4 Velocity profile and flowrate ratio of the original point set and their analytical approximation

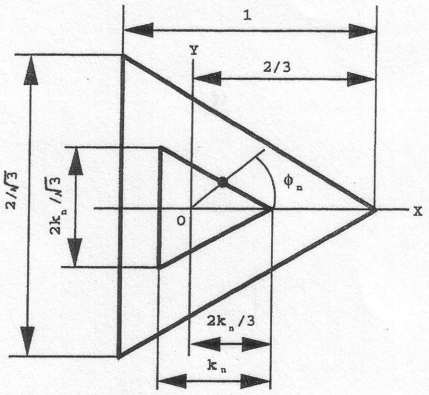

Fig. 5 Geometry of the triangular cross section of jet flow

For laminar jetflow, the average velocity profile of particles is assumed to be similar to that of one-phase waterjet. This assumption is based on the experimental discovery that the similarity exists between the average velocity profiles of particles and their transporting medium (e.g., Alajbegovc et al., 1994). In addition, two important points should be emphasized here for this assumption. (*i*) The average velocity profile is chosen for obtaining a group of one-to-one mapping equations through Eq. (15), the unpredictable or chaotic properties of particles in the new source will not be changed because they are relevant to appearing positions and orders with respect to each other. As a matter of fact, the oscillating characteristic of the factual velocity profile for a new source, like the old one shown in Fig. 4, will always retain due to the disordered property. (*ii*) The average velocity profile can be any desired form, numerical or analytical, which depends on the practical needs.

From known results in fluid mechanics (Shames, 1962 and Currie, 1992), one can find

$$\bar{V}_z = 1 - \beta(x, y) \tag{16}$$

where

$$\beta(x, y) = \frac{x^2}{a^2} + \frac{y^2}{b^2} \quad \text{(elliptical flow)} \tag{17}$$

$$\beta(x, y) = \frac{27}{4a^2}\left[x^2 + y^2 - \frac{x}{a}(x^2 - 3y^2) \right] \quad \text{(equilateral triangular flow)} \tag{18}$$

$$\beta(x, y) = \frac{4}{b^2}\left[x^2 + \frac{8b^2}{\pi^3} \sum_{m=1,3,5}^{\infty} (-1)^{(m-1)/2} \times \frac{\operatorname{ch}\left(\frac{m\pi}{b} y\right) \cos\left(\frac{m\pi}{a} x\right)}{m^3 \operatorname{ch}\left(\frac{m\pi a}{2b}\right)} \right] \quad \text{(rectangular flow)} \tag{19}$$

where a and b are constants. As shown in Fig. 5, an analytical result is given here for equilateral triangular flow as an illustrative example. From (13) and (14) one can get

$$\left(\iint_{S_{xy}} V_z^* ds \right) \Big/ \left(\iint_{S_0} V_z^* ds \right) = \frac{(\theta_n + \pi)}{2\pi} [1 - (1 - r_n)^{11/10}(1 + \tfrac{11}{10} r_n)] \quad (-\pi \le \phi_n < \pi) \tag{20}$$

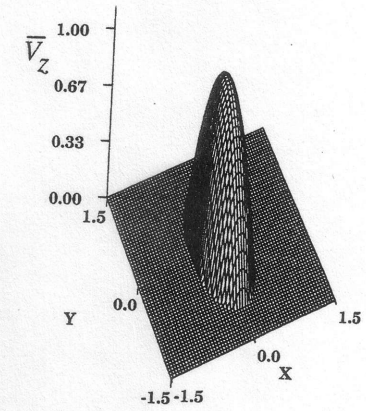

(a)

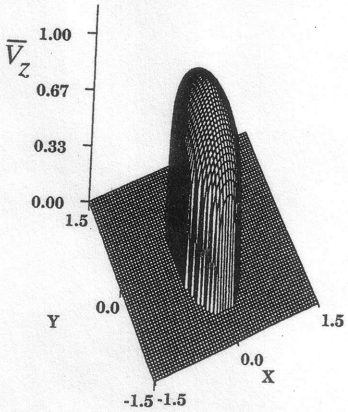

(b)

Fig. 6 Average velocity profiles of elliptical flow. (*a*) Laminar flow. (*b*) Turbulent flow.

where (r_n, θ_n) are the polar coordinates of the nth particle in f_p. After substitution of (18) into the right side of (15), tedious calculations lead to

$$\left(\iint_{\bar{S}_{xy}} \bar{V}_z ds\right) \Big/ \left(\iint_{\bar{S}_0} \bar{V}_z ds\right) = k_n^2 \Phi(\phi_n)$$

$$(0 \le k_n \le 1) \quad (21)$$

where

$$\Phi = \frac{1}{2} + \frac{4 \tan \phi_n (3\sqrt{3} + 27 \tan \phi_n + 14\sqrt{3} \tan^2 \phi_n)}{81(1 + \sqrt{3} \tan \phi_n)^3}$$

$$(0 \le \phi_n \le 2\pi/3) \quad (22)$$

$$\Phi = \frac{5}{6} + \frac{\sqrt{3} \tan \phi_n (21 - \tan^2 \phi_n) + 54}{324}$$

$$(2\pi/3 \le \phi_n \le \pi) \quad (23)$$

$$\Phi = \frac{1}{6} + \frac{27 - 69\sqrt{3} \tan \phi_n + 135 \tan^2 \phi_n - 25\sqrt{3} \tan^3 \phi_n}{81(1 - \sqrt{3} \tan \phi_n)^3}$$

$$(-2\pi/3 \le \phi_n \le 0) \quad (24)$$

$$\Phi = \frac{\tan \phi_n (21 - \tan^2 \phi_n)}{108\sqrt{3}} \quad (-\pi \le \phi_n \le -2\pi/3) \quad (25)$$

In terms of (15, 20, 21), two mapping equations for determining two variables k_n and ϕ_n of Eq. (21) are of forms

$$k_n = [1 - (1 - r_n)^{11/10}(1 + \tfrac{11}{10} r_n)]^{1/2} \quad (26)$$

$$\Phi(\phi_n) = \frac{\theta_n + \pi}{2\pi} \quad (27)$$

The coordinates (x_n, y_n) of the nth particle in triangular point set $\bar{f}_p$ are ascertained by

(a) $0 \le \phi_n \le 2\pi/3$:

$$y_n = x_n \tan \phi_n = \frac{2k_n}{3(1 - \sqrt{3} \tan \phi_n)} \tan \phi_n \quad (28)$$

(b) $-2\pi/3 \le \phi_n \le 0$:

$$y_n = x_n \tan \phi_n = \frac{2k_n}{3(1 + \sqrt{3} \tan \phi_n)} \tan \phi_n \quad (29)$$

(c) $-\pi \le \phi_n \le -2\pi/3$ and $2\pi/3 \le \phi_n \le \pi$:

$$x_n = -\frac{k_n}{3}, \; y_n = -\frac{k_n}{3} \tan \phi_n \quad (30)$$

Mapping functions for other types of flow are not given here for brevity, but the following simulation processes will use results for elliptical jetflow. It can be seen from (22–30) that the unpredictable behavior inherited from the original one still remains in the new one.

The seventh-root law (Shames, 1962) for the average velocity profile of an axisymmetrical turbulent pipe flow is extended to describe noncircular flow. That is, the general average velocity profile for noncircular turbulent jetflow is given by

$$\bar{V}_z = (1 - \sqrt{|\beta(x, y)|})^{1/7} \quad (31)$$

where $\beta(x, y)$ is ascertained by (17–19) for different nozzle shapes. Two patterns are displayed in Figs. 6(a, b), to show the difference between two types of elliptical jetflow.

Equation (31) is considered to be valid if it can generate the sharp change of velocity gradients near the nozzle wall, similar to many experimental results for both one-phase or multiphase flow (Shame, 1962; Lee and Durst, 1982; Alajbegovic, 1994). The concern over the shape of the velocity profile arises because it is relevant to the cutting quality of AWJ. As stated above, one can choose any velocity profile as the average one for a new particle source based on practical needs. Two approaches are designed to ensure the completeness of creating new particle sources. Theoretically, a feedback control algorithm is developed for checking the consistency between the defined velocity profile and the factual velocity profile of particles. Experimentally, the shapes of holes drilled by AWJ are compared with simulation results (Yong and Kovacevic, 1997d). Very good agreement is confirmed between theory and experiment.

3 Simulation of AWJ Machining

During simulation of an AWJ machining process, according to previous results, the relation between the average penetration depth δh_n generated by the nth particle and other parameters is defined by

$$\delta h_n = c_1 [V_z(x_n, y_n)]^s \quad (32)$$

where the exponent s is taken as 2 in the following simulation, c_1 is a constant determined by the test of one on-line cut, and $V_z(x_n, y_n)$ is the dimensionless normal velocity of the particle at an instant t. The time is measured by abrasive flowrate $\dot{m}$.

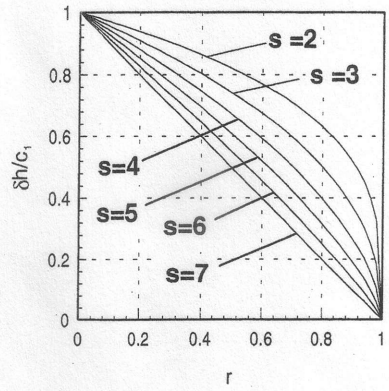

(a)

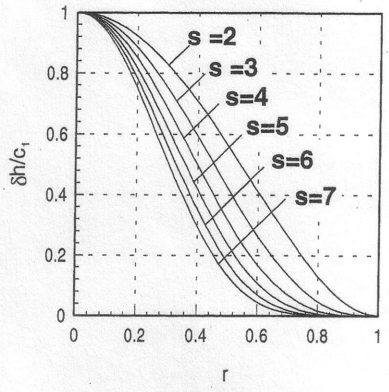

(b)

Fig. 7 The possible shapes of the kerf 's bottom derived from the constitutive equation for erosion rate. (*a*) Turbulent velocity profile. (*b*) Laminar velocity profile.

For example, 10^4th particle strikes the surface at the 0.5 second if $\dot{m} = 2 \times 10^4$ (particles)/s. Equation (32) does not specify the influences of individual parameters, such as the impact angles, the possible rotation and the geometry of a particle, due to the following reasons:

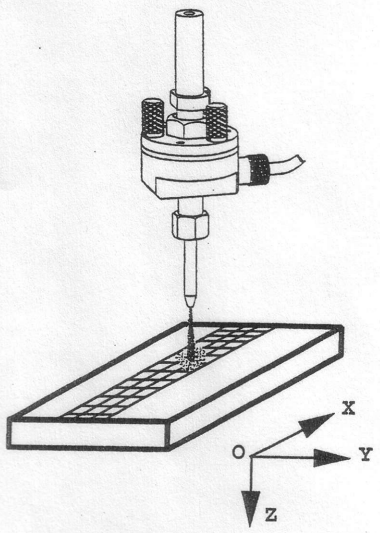

Fig. 8 Illustration of the memory cell approach

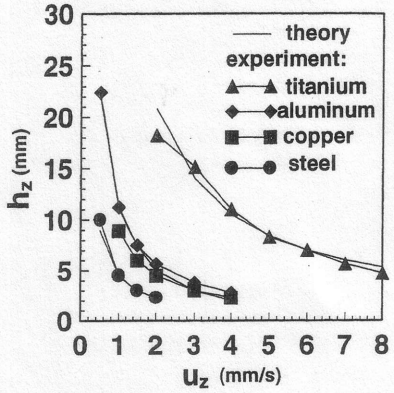

Fig. 9 Comparison between theory and experiment for cutting different materials (circular jet)

- The macro erosion rate of particles depends mainly on velocities and the number of particles striking the surface. Usually, a very small area can experiences thousands of impacts from particles.
- It is impractical to instantly measure angles and rotations of millions of particles in a few seconds under the harsh machining environment.
- A brief equation is more efficient for either off-line simulation or on-line control (Kovacevic, 1992) after its accuracy is confirmed by experiments.

More importantly, the constant c_1 of Eq. (32) acts as a synthetic parameter that can reflect the influences of different parameters in a sense of average measurement.

How to determine the value of the exponent s has long been an interesting subject when only the erosion rate of one single particle is analyzed. Nevertheless, this issue becomes less influential when millions of different particles and their velocities are all taken into account. Some findings are introduced as follows.

In the present model, the maximum depth of drilling is independent of the exponent s according to

$$(\delta h_i)_{\max} = c_1[V_{z\max}(x_i, y_i)]^s = c_1 \quad (V_{z\max}(x_i, y_i) = 1). \tag{33}$$

As a result, the maximum depth h_z at the center of a hole has the form

$$h_z = \sum_{j=1}^{J} \delta h_j = \sum_{j=1}^{J} c_1 = Jc_1 \tag{34}$$

where J is the number of particles hitting the given point. In this circumstance, the variation of s is irrelevant to the calculation of

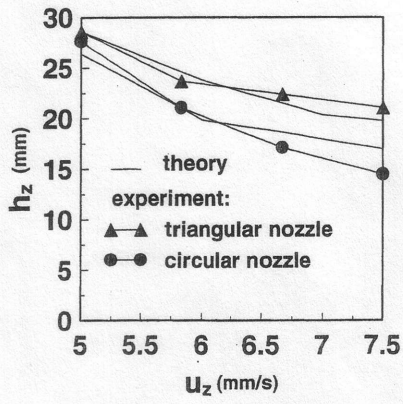

Fig. 10 Comparison between theory and experiment for cutting different materials (triangular jet)

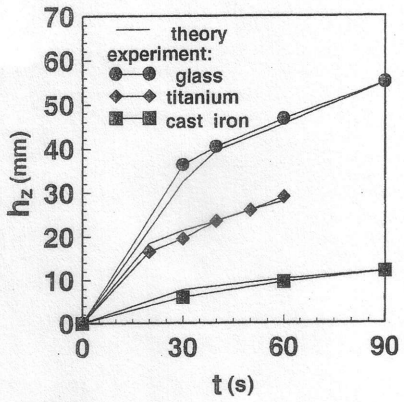

Fig. 11 Comparison between theory and experiment for drilling titanium, glass, and cast iron

h_z. So long as the value of c_1 is determined by a drilling test, the maximum depth for a material depends solely on the total number of particles striking the given area. The exponent s does lead to changes on the shape of a kerf through changing the erosion rate. However, the value range of $n = 2 \sim 3$ here proves to be more reasonable. Because the shape of a kerf on the cross section of a workpiece is similar to the curve given by Eq. (32), the possible shapes of a kerf are plotted in Figs. 7 (a, b). Experiments show that the shape of a kerf matches well with the curves obtained with $n = 2 \sim 3$. Other shapes of kerfs are rarely seen in practical situation, particularly, $n = 5 \sim 7$ for turbulent flow.

A memory technique is introduced to record quantities and kinematic histories of particles passing through a given area of the workpiece to be cut, as explained in Fig. 8. When the particle jetflow with a moving nozzle travels over the erosion region, the erosion rates in different parts of the region greatly differ. The region is divided into a network, and each element of the network serves as a memory cell to record the histories of particles passing through it. Their penetration abilities are evaluated by use of Eq. (32). The final shape of a kerf is the accumulation of results of all the cells over the erosion region. Major simulation parameters are listed as follows

- traverse rate of a nozzle $u_z = 0.5 \sim 4.0$/s (length unit/second)
- particle flowrate $\dot{m} = 2 \sim 8 \times 10^4$/s (particle number/second)
- dimensionless radius of the nozzle $r_z = 1$ (length unit) for the circular nozzle

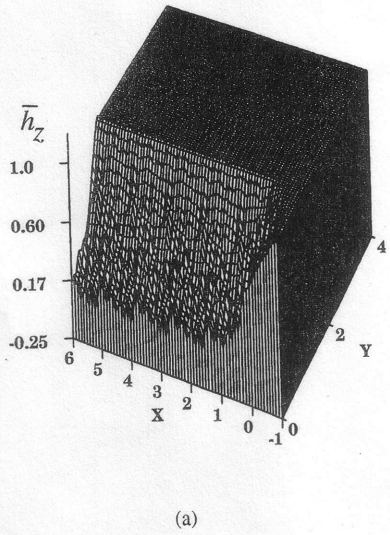

(a)

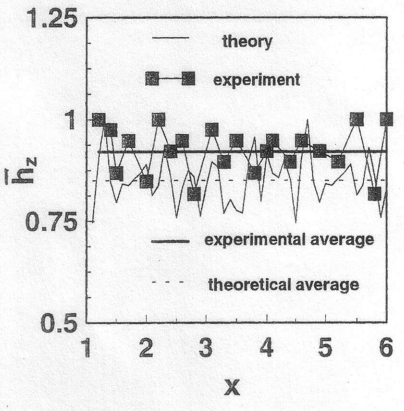

(b)

Fig. 12 Evaluation of roughness. (*a*) 3D configuration of bottom surface roughness. (*b*) A comparison between theory and experiment.

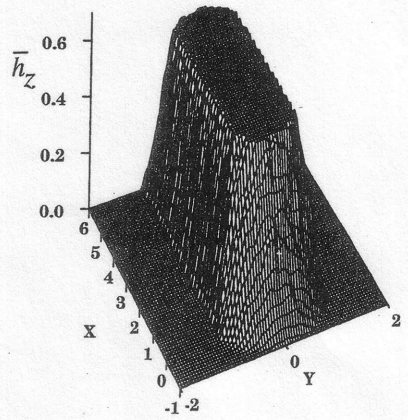

(a)

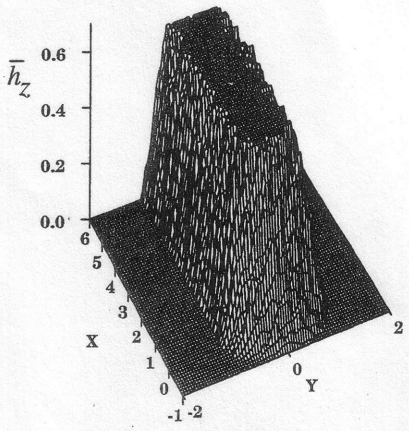

(b)

Fig. 13 3D configuration of kerfs. (*a*) u_z = 0.5 mm/s. (*b*) u_z = 4.0 mm/s.

- area of a memory cell $a_{xy} = 0.1 \times 0.1$ (length × length)
- dimensionless depth of cut $\bar{h}_z = h_z/h_{z\max}$ (h_z-depth of cut in a cell)
- total cutting length $L = 7$ (length unit) with no mask protection
- rotation angles of an elliptical nozzle $\gamma_z = 0 \sim 2\pi$
- ratio of the minor axis to the major axis of an elliptical nozzle $b/a = 0.5/1.0$.

In tests carried out by the authors, experimental conditions vary with workpiece materials, including waterjet pressure, abrasive flowrate and size and material, nozzle diameter and standoff distance. They are not all listed for brevity but are available on request.

3.1 Simulation of Cutting. The cutting simulation is conducted for titanium, annealed aluminum, carbon steel, and cooper. As shown in Fig. 9, the consistency between theory and experiment justifies the validity of the model along with constitutive Eq. (32). The depth of cut is obviously a nonlinear function of nozzle speed u_z. At this point, the model proves to be very competitive with other models because only one cut is needed to determine a physical constant in Eq. (32). Moreover, other models break down when the nozzle shape is no longer a circular one. A comparison between equilateral triangular and circular jetflow is given in Fig. 10 where experimental data were given by Rankin and Wu (1995) from cutting aluminum. One advantageous feature of the present model is that any shape of jetflow can be simulated without principle difficulty.

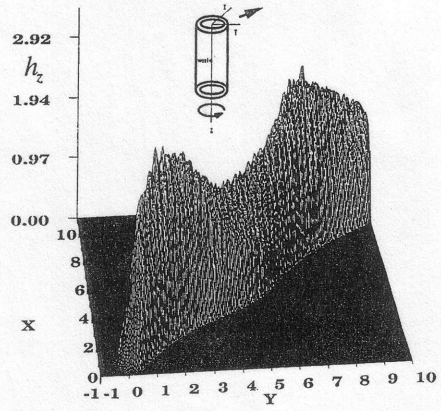

Fig. 15 3D configuration of a cut generated by a rotating and moving elliptical nozzle

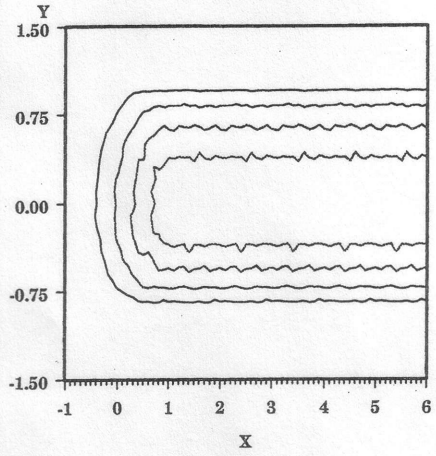

(a)

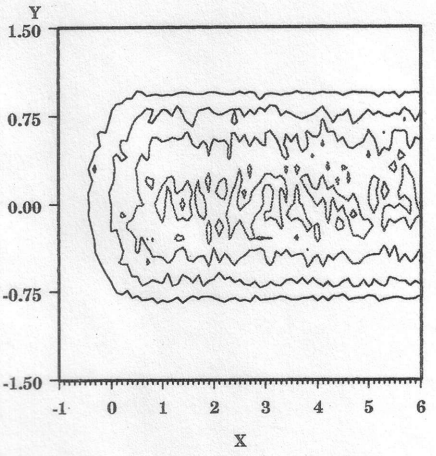

(b)

Fig. 14 Contour maps for measurement of waviness. (*a*) $u_z = 0.5$ mm/s. (*b*) $u_z = 4.0$ mm/s.

3.2 Simulation of Drilling. The constitutive equation for drilling differs from Eq. (32) because of potential damping effects with the increase in depth of drilling (Yong and Kovacevic, 1997d). Still, only one physical constant involves the estimation of erosion rates. A comparison between theoretical and experimental results is plotted in Fig. 11 for drilling titanium, glass and cast iron, for ductile, brittle and quasi-brittle materials. It follows that the drilling model has very good accuracy.

3.3 Simulation of Roughness and Waviness. As indicated earlier, previous models failed to reflect parameters of surface quality, such as roughness and waviness, because they are caused mostly by distinct kinematic features of millions of particles, nozzle shape, travel speed, etc.. A theoretical 3D configuration that shows the roughness on the bottom of a kerf is displayed in Fig. 12(*a*). The roughness results from the irregularity of the depth. A comparison between theory and experiment is given in Fig. 12(*b*) where the experimental counterpart of Fig. 12(*a*) is obtained by measuring the depth of cut on an aluminum specimen. In simulation, the traverse speed u_z of the nozzle is $u_z = 2.0$ mm/s and the abrasive flowrate is $\dot{m} = 8 \times 10^4$ (particles/s). Calculations show that the error between theoretical average and experimental depths is 7.6 percent.

Many experiments have demonstrated that very severe waviness occurs on the lateral surfaces of a workpiece when the travel speed of the nozzle increases from 0.5 mm/s to 4.0 mm/s (e.g., Hashish, 1992). However, previous models are incapable of including the intrinsic surface feature in association with other 3D parameters. Figures 13(*a*, *b*) are 3D configurations of two cuts corresponding to $u_z = 0.5$ mm/s and $u_z = 4.0$ mm/s, respectively. The waviness on the lateral surfaces is clearly visible in Fig. 13(*b*). Relative quantitative waviness of a cut can be determined by employing the contour map of a 3D configuration as displayed in Figs. 14(*a*, *b*) where the dimensionless heights of contours are 0.2, 0.4, 0.6, and 0.8. Note that at the different depth of cut the waviness is different. For example, results show that at the height $\bar{h}_z = 0.6$, the surface waviness w_z changes from $w_z = 0.18$ to $w_z = 0.65$ when the traverse speed of a nozzle increases from 0.5 mm/s to 4.0 mm/s. Experimental verification of theoretical waviness involves many sophisticated techniques and it will be discussed in a separate paper.

3.4 Simulation of Rotating Nozzle. The above discussions aim at the simulation of well-known phenomena in AWJ machining. In fact, the present model can be applied to explore many new functions of AWJ. Here is an example for producing the curved depth of cut which is one of the most important topics in the AWJ machining area and no mature method has been found yet to date. The strategy used here is to use a moving and rotating elliptical nozzle in association with, if necessary, the mask technique. The 3D cutting configuration is displayed in Fig. 15. Clearly, this is a potential method to control the depth of cut.

4 Conclusion and Discussion

3D abrasive machining is an expensive and time-consuming process, especially when an innovation needs to be justified. The cost may not pay off in many cases mainly because many parameters influence the machining outcome. For example, when a noncircular nozzle is applied to the shop floor, engineers and researchers have to get through lengthy experiments to verify its validity by changing machining conditions, such as the orientation and traverse speed of the nozzle, the water pressure, the flowrate of abrasives and so on. This makes it very difficult to find optimal parameters for a specific purpose.

Simulation is possibly the best way to solve the problem. In the present work, fractal point sets with chaotic behavior are employed to represent particles on the cross section of jetflow. These point sets can be endowed with any velocity profile and shape to meet practical needs. One of the most important functions carried by the model is that it is capable of simulating general motion of a nozzle on which many operations on the shop floor rely. The cutting, drilling, evaluation of surface quality, innovation of nozzle shape and the depth control are reported in this paper and selective experiments are conducted to verify its effectiveness and accuracy. Results confirm that it is a robust model and has potential to be an industrially applicable one.

In this research, less attention is paid to the investigation of constitutive equations for different working environments. This does not mean, however, that this topic is not worth further consideration. As a matter of fact, many subjects relevant to this topic have probably not been addressed so far, such as the dynamic property of workpiece material subjected to very localized impact loading or the influence of strain rates, multi-impacts of chaotic particles, instability of particles due to the loss of penetration ability, etc.. According to the results reported in this work, a classical formulas developed previously performs accurately for the most common AWJ machining process, such as cutting and drilling.

Acknowledgment

The authors would like to thank the National Science Foundation for the support of this project under Grant DMI-9523010. The appreciation is extended to the Allison Engine Company, United Technologies Pratt & Whitney, and the Flow International Corporation for their support as the cosponsors.

References

Alajbegovic, A., et al., 1994, "Phase Distribution and Turbulence Structure for Solid/Fluid Upflow in a Pipe," *Int. J. Multiphase Flow,* Vol. 20, pp. 453–479.

Bitter, J. G. A., 1963, "A Study of Erosion Phenomena—Part I," *Wear,* Vol. 16, pp. 5–21.

Bitter, J. G. A., 1963, "A Study of Erosion Phenomena—Part II," *Wear,* Vol. 16, pp. 169–190.

Currie, I. G., 1992, *Fundamental Mechanics of Fluid,* McGraw-Hill, New York.

Finnie, I., 1958, "The Mechanisms of Erosion of Ductile Metals," *Proceedings of the Third National Congress of Applied Mechanics,* ASME, pp. 527–532.

Finnie, I., 1960, "Erosion of Surfaces by Solid Particles," *Wear,* Vol. 3, pp. 87–103.

Gulden, M. E., 1979, "Solid Particle Erosion of High Technology Ceramics," ASTM STP664, W. F. Afler, ed., pp. 101–122.

Hashish, M., 1984, "A Modeling Study of Metal Cutting with Abrasive-Waterjets," ASME *Journal of Engineering Materials and Technology,* Vol. 106, pp. 88–100.

Hashish, M., 1992, "Three Dimensional Machining with Abrasive Waterjet," *Jet Cutting Technology,* Vol. 13, pp. 605–620.

Hashish, M., 1994, "Controlled-Depth Milling Techniques Using Abrasive Waterjet," *Jet Cutting Technology,* Vol. 13, 449–461.

Hongawa, H., et al., 1992, "Annular Jet and Its Applications," *Journal of Jet Technology Society of Japan,* Vol. 9, pp. 1–11 (in Japanese).

Hutchings, I. M., 1979, "Mechanisms of the Erosion of Metals by Solid Particles," ASTM STP 664, *Erosion: Prevention and Useful Applications,* pp. 59–76.

Kovacevic, R., 1992, "Monitoring of Depth of Abrasive Waterjet Penetration," *Int. J. Mach. Tools Manufact.,* Vol. 1, pp. 55–72.

Lee, S. L. and Durst, F., 1982, "On the Motion of Particle in Turbulent Duct Flow," *Int. J. Multiphase Flow,* Vol. 8, pp. 125–146.

Neilson, J. H., and Gilchrist, 1968, "Erosion by a Stream of Solid Particles," *Wear,* Vol. 11, pp. 111–122.

Rankin, G. J. and Wu, S. S., 1995, "Abrasive Waterjet Cutting with a Shapejet," *Proceeding of 7th American Water Jet Conference,* Houston, Texas, pp. 219–228.

Shames, I. H., 1962, *Mechanics of Fluids,* McGraw-Hill, New York.

Tilly, G. P., and Sage, W., 1970, "The Interaction of Particle and Material Behavior in Erosion Processes," *Wear,* Vol. 16, pp. 447–465.

Yong, Z., and Kovacevic, R., 1997a, "Effects of Water-Mixture Film on Impact Contact in Abrasive Waterjet Machining," *International Journal of Mechanical Science,* Vol. 39, pp. 729–739.

Yong, Z., and Kovacevic, R., 1997b, "Fundamentals of Constructing Particle-Laden Flow by Fractal Point Sets and Predicting 3D Solid Erosion Rates," *International Journal of Chaos, Solitons and Fractals,* Vol. 8, pp. 207–220.

Yong, Z., and Kovacevic, R., 1997c, "Feedback Control of Chaotic Point Sets with Arbitrary Velocity Profile," in press.

Yong, Z., and Kovacevic, R., 1997d, "Modeling of Jetflow Drilling with Consideration of Chaotic Erosion Histories of Particles," *Wear,* in press.

Zeng, J., and Kim, T. J., 1992, "Development of an Abrasive Waterjet Kerf Cutting Model for Brittle Materials," *Jet Cutting Technology,* Vol. 13, pp. 483–501.